HER2 Expression in Breast Cancer Cells Is Downregulated Upon Active Targeting by Antibody-Engineered Multifunctional Nanoparticles in Mice

Fabio Corsi,[†,∥] Luisa Fiandra,[†,∥] Clara De Palma,[†] Miriam Colombo,[†,‡] Serena Mazzucchelli,[†] Paolo Verderio,[‡] Raffaele Allevi,[†] Antonella Tosoni,[†] Manuela Nebuloni,[†] Emilio Clementi,[†,§] and Davide Prosperi[‡,⊥,*]

[†]Dipartimento di Scienze Cliniche "Luigi Sacco", Università di Milano, Ospedale L. Sacco, via G.B. Grassi 74, 20157 Milano, Italy, [‡]Dipartimento di Biotecnologie e Bioscienze, Università di Milano-Bicocca, piazza della Scienza 2, 20126 Milano, Italy, [§]Istituto Scientifico Eugenio Medea, 23842 Bosisio Parini, Italy, and [⊥]Laboratorio di Biofisica e Nanomedicina, Polo Tecnologico, Fondazione Don Gnocchi IRCCS-ONLUS, 20148 Milan, Italy. [∥]These authors contributed equally to the research.

ABSTRACT Subcellular destiny of targeted nanoparticles in cancer cells within living organisms is still an open matter of debate. By *in vivo* and *ex vivo* experiments on tumor-bearing mice treated with antibody-engineered magnetofluorescent nanocrystals, in which we combined fluorescence imaging, magnetic relaxation, and trasmission electron microscopy approaches, we provide evidence that nanoparticles are effectively delivered to the tumor by active targeting. These nanocrystals were demonstrated to enable contrast enhancement of the tumor in magnetic resonance imaging. In addition, we were able to discriminate between the fate of the organic corona and the metallic core upon cell internalization. Accurate immunohistochemical analysis confirmed that hybrid nanoparticle endocytosis is mediated by the complex formation with HER2 receptor, leading to a substantial downregulation of HER2 protein expression on the cell surface. These results provide a direct insight into the pathway of internalization and degradation of targeted hybrid nanoparticles in cancer cells *in vivo* and suggest a potential application of this immunotheranostic nanoagent in neoadjuvant therapy of cancer.

KEYWORDS: magnetic nanoparticles · breast cancer · tumor targeting · imaging · ligand–receptor recognition · theranostic agent

A primary goal in cancer diagnostics is to develop molecular contrast agents that identify the presence of a malignant tumor at early stages, track possible migration of tumor cells, and monitor tumor response to surgical or pharmacological treatments.[1−3] The diagnosis of axillary localization of breast cancer metastases is at present essentially based on highly invasive and seldom conclusive detection methods, often requiring the sentinel lymph node dissection.[4] In this context, a primary challenge is the design of new tools allowing easy, reliable, and noninvasive identification of lymph node metastases. A possible strategy resides in the development of new target-specific multifunctional tracers capable of optimizing breast cancer diagnosis *in vivo* by combining low-invasive fluorescence techniques and magnetic resonance imaging (MRI).[5] In the past decade, nanotechnology has provided new tools in this direction. In particular, the development of a new generation of multifunctional hybrid organic/inorganic nanomaterials, including iron oxide nanoparticles, held great promises for diagnosis and treatment of malignant tumors.[6,7]

A broad range of new synthetic strategies for iron oxide nanoparticles have been reported, enabling fine-tuning of size, shape, and magnetic properties.[8] Recently, novel biofunctionalization approaches have been successfully attempted to improve the nanoparticle stability in physiological media and to gain a control on tight immobilization, distribution, and suitable orientation of target ligands on the nanoparticle surface, which is essential for optimizing the targeting efficiency toward cell receptors.[9−12] Several *in vivo* studies have demonstrated the potential of targeted iron oxide nanoparticles as local enhancers of MRI contrast, and the first clinical trials conducted on patients bearing metastatic lymph nodes have provided promising perspectives.[13,14] From these studies, a crucial point has emerged and still needs to be thoroughly examined, that is, the targeting mechanisms and the fate of the different components of hybrid nanoparticles when they have reached their final destination. Although a few investigations have provided important data with cell cultures,[15] the molecular features of the interaction of hybrid nanoparticles with cells and tissues *in vivo* remain unexplored. In

* Address correspondence to davide.prosperi@unimib.it.

Received for review April 29, 2011 and accepted July 26, 2011.

Published online July 26, 2011
10.1021/nn201570n

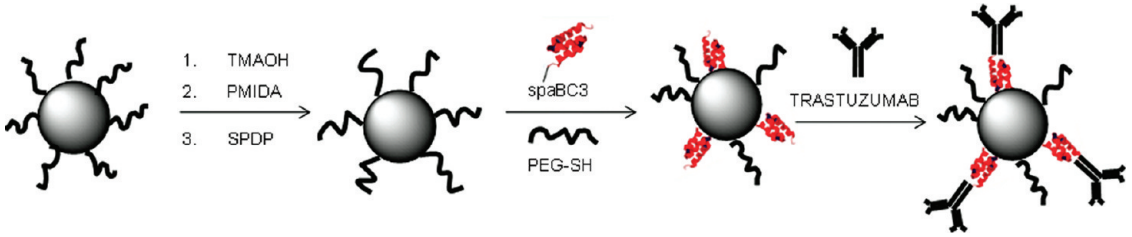

Scheme 1. Step sequence for the preparation of TMNC.

particular, it is still a matter of debate whether functionalization with homing ligands is able to guide nanoparticles to the tumor by active targeting also in living organisms, or nanoparticle delivery is rather mediated by passive transport *via* opsonization and/or macrophage incorporation.[16,17]

Recently, we have designed a versatile molecular nanohybrid suitable for site-specific immobilization of antibodies.[18] This nanocomplex was a magnetite nanocrystal conjugated with a recombinant low molecular weight monodomain of protein A, which exhibited a strong affinity for human and rabbit IgG molecules. Magnetic nanocrystals conjugated to the commercial anti-HER2 monoclonal antibody trastuzumab (TMNC) were demonstrated to be effective in selectively recognizing the "human epidermal growth factor receptor 2" (HER2) expressed in MCF-7 breast cancer cells in cultures. HER2 is a membrane tyrosine kinase receptor belonging to the family of the erbB and is overexpressed in 25−40% of human mammary carcinomas. HER2 regulates cell growth, adhesion, migration, and cell differentiation and is referred to as an "orphan" receptor because no known endogenous ligand has yet been identified.[19,20]

In the present work, we have improved the preparation of TMNC for *in vivo* application, allowing us to carry out a careful investigation of their targeting efficiency and biodistribution by combining MRI monitoring, highly sensitive epifluorescence tracking of TMNC in Balb/c nude mice bearing MCF-7 cells, and accurate tissue analyses. The results we are presenting here provided a new insight into the fate of the individual components of the hybrid nanocomposites once they reached the target cells *in vivo*. In order to track the organic moiety separately from the metal core, we preferred to label only trastuzumab (Tz) with AlexaFluor660 (AF660), rather than making the nanoparticle entirely fluorescent.

Due to the targeting efficiency of antibodies, IgG-functionalized nanoparticles have found broad interest for application in cancer diagnosis and as carriers of chemotherapeutic agents for the treatment of malignant tumors.[21−23] A further aim of this work was to investigate the potential of TMNC as a neoadjuvant agent for combination therapy of breast cancer exploiting the attitude of Tz to inhibit the signaling processes triggered by HER2 overexpression.

RESULTS AND DISCUSSION

Optimization of TMNC Synthesis for *In Vivo* Studies. The original procedure for the synthesis of TMNC involved a nanocrystal controlled nucleation and growth by solvothermal decomposition in the presence of oleic acid followed by ligand exchange with *N*-phosphonomethyl iminodiacetic acid phosphonate (PMIDA), which led to a dispersion soluble in the aqueous phase. The ligand was modified by condensation with 2,2′-(ethylenedioxy)bis(ethylamine) (EDBE) and further functionalized with *N*-succinimidyl-3-[2-pyridyldithio]propionate (SPDP). The resulting thiol-reactive PDP functionalities were exploited for the conjugation with a recombinant Cys_3-ended single-domain variant of protein A (spaBC3), capable of capturing IgG molecules by strong binding with their Fc fragment.[18] SpaBC3 allowed for the tight immobilization of Tz in the optimal orientation for binding to HER2. TMNC proved to be long-term stable in several buffered media and thus suitable for studies with cell cultures. However, when we explored the possibility of using TMNC for intravenous administration, they invariably showed a tendency to accumulate at the mouse tail, in correspondence to the site of injection. After having thoroughly checked each step of the synthetic procedure in terms of particulate stability, we found that the critical step was the ligand exchange. Hence, we improved the phase transfer by an intermediate reaction with tetramethylammonium hydroxide (TMAOH), which led to the same final antibody nanocomplex dramatically reducing the TMNC localization at the site of injection, as it was capable of diffusing quickly in the bloodstream. The complete sequence is reported in Scheme 1. Next, Tz was cross-linked to spaBC3 with glutaraldehyde to enforce the antibody grafting to the nanoparticle, which unfortunately resulted in particle aggregation. Thus, we evaluated the spontaneous release of Tz labeled with AF660 from TMNC in serum to assess the tightness of Tz−spaBC3 binding under physiological conditions, and we did not find any traces of released Tz after 1 week at 37 °C. Hence, we decided to utilize the optimized TMNC for the *in vivo* studies.

HER2-Positive Tumor Imaging with AF660-TMNC. MCF-7 breast cancer cells were grown subcutaneously in Balb/c nude mice. Once the tumor reached the size of approximately 1 cm of diameter, 5 μg/g body weight of AF660-TMNC was injected in mice by the tail vein,

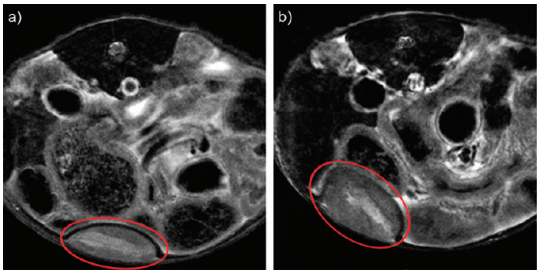

Figure 1. Monitoring of TMNC uptake *in vivo* by MRI. The axial T_2-weighted MR images have been obtained from MCF-7 tumor-bearing mice (a) before and (b) 24 h after the injection of nanocrystals. The images, obtained by a T_2-mapping sequence, were acquired at 32.2 ms echo time.

and their localization in the MCF-7 tumor was monitored 24 h after injection by MRI to assess their potential as targeted contrast agent for the detection of HER2-positive breast cancer cells *in vivo*. T_2-weighted axial images of a tumor-bearing mice acquired pre-injection (Figure 1a, control) and 24 h postinjection (Figure 1b) of TMNC exhibited an increase in negative contrast in correspondence to MCF-7 xenograft (red circle) caused by nanocrystal accumulation at the tumor. A remarkable decrease in T_2* maps was also observed in the tumor region at 24 h (Figure S2 in Supporting Information). To confirm the specificity of targeting after antibody conjugation, control MRI images were acquired with PEG-coated MNCs (Figure

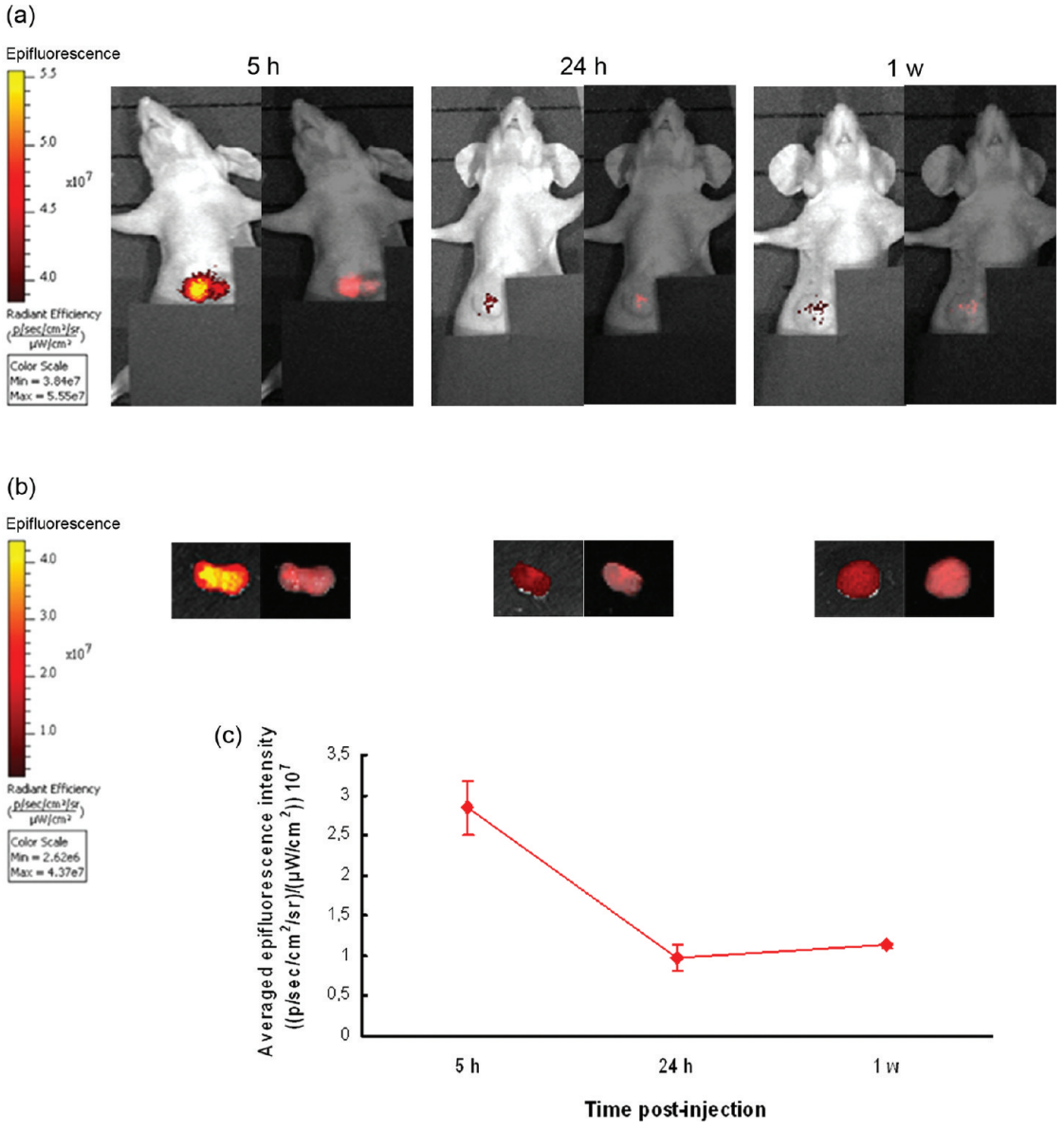

Figure 2. CCD camera images of mice bearing MCF-7 xenografts (a) and of the isolated tumors (b) at 5 h, 24 h, and 1 week postinjection of AF660-TMNC. Epifluorescence intensity images and spectrally unmixed fluorescence images are reported on left and right, respectively. (c) Averaged epifluorescence intensity of isolated tumors. Mean ± SE of three different samples for each experimental time.

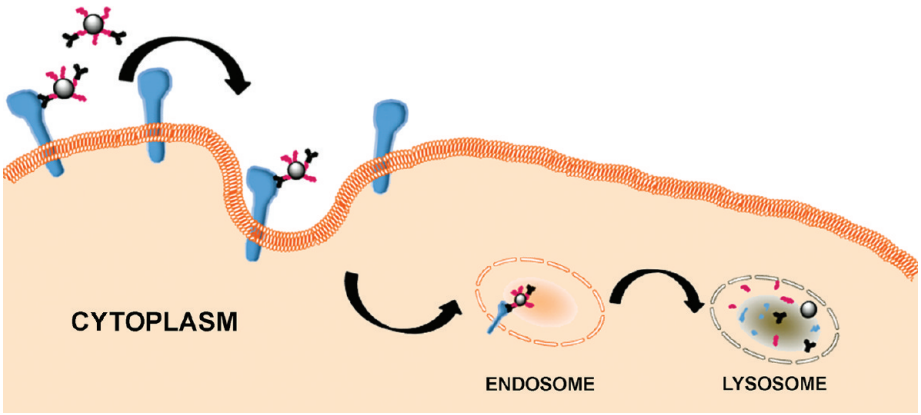

Scheme 2. Mechanism of TMNC internalization and degradation in HER2-positive MCF-7 cells. In a first step, TMNC binds to HER2 membrane receptors, inhibiting homodimer formation. Next, the TMNC−HER2 complex formation triggers the local membrane invagination, followed by the complex incorporation within internal early endosomes, which evolve in late endosomes and, eventually, in lysosomes, where the organic corona is rapidly degraded. This process results in a reduced surface expression of HER2 receptor.

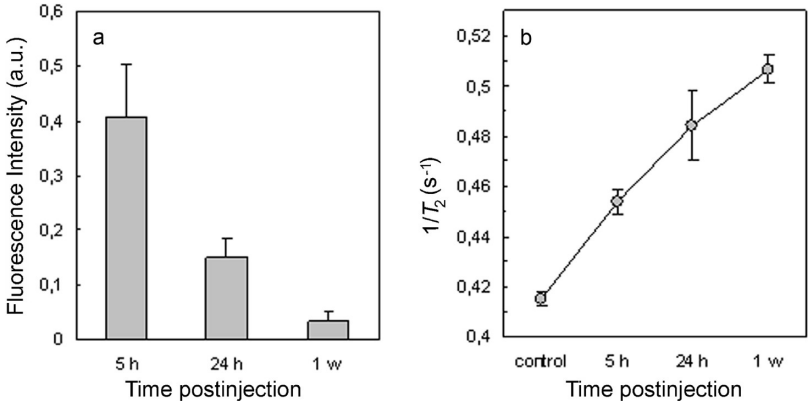

Figure 3. Fluorescence intensity (a) and inverse relaxation time (b) of MCF-7 lysates, at 5 h, 24 h, and 1 week postinjection of AF660-TMNC. Mean ± SE of three different samples.

S3). Next, epifluorescence (Epf) images of supine mice, obtained with a CCD camera (IVIS Lumina II, Calipers Life Sciences, UK) at 5 h, 24 h, and 1 week after injection, confirmed the capability of AF660-TMNC to target the HER2-positive tumors (Figure 2a). The maximal Epf emission in xenografts was observed at 5 h, while the signal intensity in the tumor unexpectedly decreased after 24 h. *Ex vivo* analysis of Epf in isolated tumors confirmed the maximal signal intensity at the shorter time of exposure (Figure 2b), as also indicated by the averaged Epf intensity, reported in Figure 2c as the mean value from three different tumors for each experimental condition. The drop in Epf was initially attributed to the surface-weighted properties of Epf imaging, which usually allows for an optimal detection sensitivity but is strongly limited by the short penetration depth of photons, which is dependent on diffusion time, as previously observed.[24] Nevertheless, we could not exclude that the fall of fluorescence observed by CCD images could, at least partially, reflect the degradation of the organic corona, subsequent to the receptor-mediated TMNC internalization. Indeed, the metabolization of the organic moiety, including the fluorochrome, associated with the saturation of membrane HER2 receptors, could cause an overall fluorescence decrease. This hypothesis is supported by previous evidence that one possible mechanism, by which Tz inhibits the tumor development, involves HER2 downregulation mediated by the rapid degradation of the Tz−HER2 complex upon endocytosis.[25] Such a postulated mechanism suggested that TMNC was likely to be directed to lysosomal degradation *via* receptor-mediated endocytosis triggered by formation of the Tz−HER2 complex (Scheme 2). In a recent study, Wuang *et al.* observed that the internalization of Tz-modified nanoparticles in HER2-positive breast cancer cells could be prevented by treatment with excess free Tz, which corroborates the assumption that the nanoconjugate endocytosis could be receptor-mediated.[26] Therefore, within our model, we predicted that fluorescence signal associated with the presence of Tz in TMNC would rapidly decrease, while in contrast, iron oxide would progressively accumulate inside the tumor tissue. Further investigations were needed to assess the reliability of our interpretation.

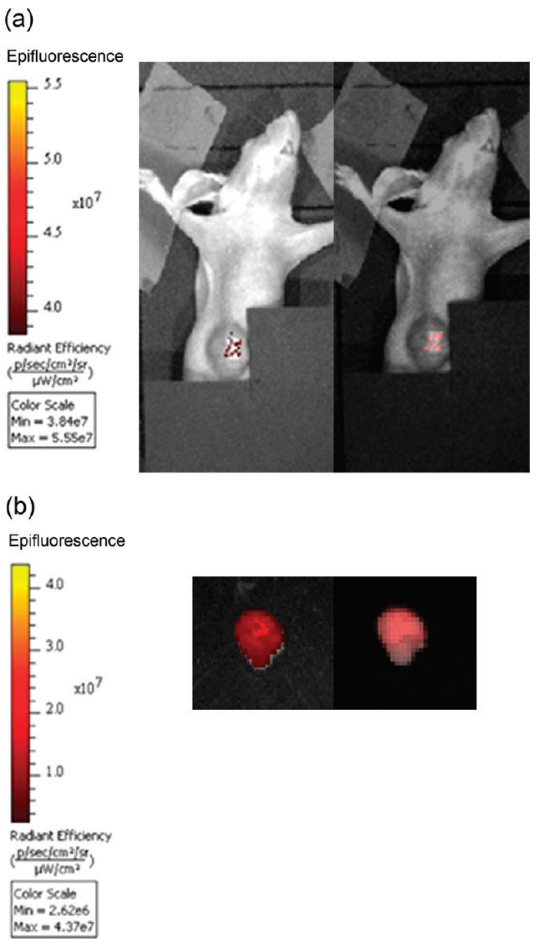

Figure 4. CCD camera images of a MDA-bearing mouse (a) and of the isolated MDA tumor (b) at 5 h postinjection of AF660-TMNC. Epifluorescence intensity images and spectrally unmixed fluorescence images are reported on left and right, respectively.

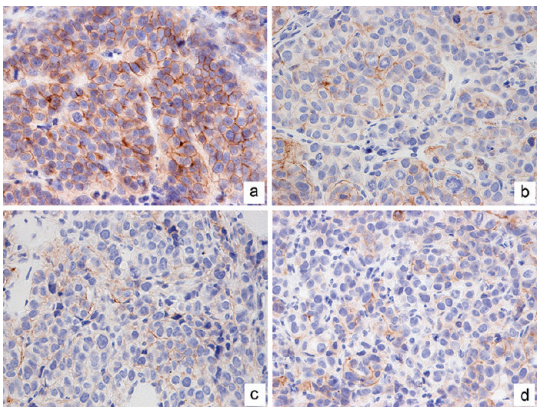

Figure 5. Immunohistochemistry of tumor section extracts before (a) and after treatment with TMNC (b–d). Samples were incubated with antibody rabbit anti-human c-erb-2 oncoprotein (1:1000 dilution, DakoCytomation), 2 h incubation. (a) Strong and diffuse membrane c-erb-2 immunostaining (score 3+) in all of the neoplastic cells. (b–d) No c-erb-2 expression is recovered in most of the neoplastic elements, with only a few c-erb-2-positive cells with diffuse (panel b, score 2+) or focal (panels c and d, score 1+) weak pattern of distribution in the tumor at 5 h, 24 h, and 1 week, respectively. Hematoxylin counterstaining, OM 40×.

Mechanism of TMNC Incorporation in MCF-7 Cells. Spectrofluorimetric assays performed on lysates of the same tumors analyzed by the CCD camera provided support to the latter interpretation, as tissue depth was not an issue in this case. Fluorescence intensity, normalized to the overall mass of proteins in each lysate, once again was maximal at 5 h and progressively decreased over time (Figure 3a). The same samples were also analyzed by magnetic relaxation measurements to assess the relative amount of iron due to the presence of magnetic nanocrystals incorporated in the tumor tissue. Magnetic relaxometry shares the same basic principle with MRI but exhibits several advantages in semiquantitative determinations, including (1) higher sensitivity, (2) it enables a direct measurement of the magnetic power of a sample, and (3) image deconvolution is not needed, which in some cases may cause artifacts. As a matter of fact, most studies making use of MRI for semiquantitative analysis require whole-body perfusion to eliminate blood interferences.[24] However, we were interested in investigating the nanoparticle distribution under normal blood flow conditions, which better reproduces the dynamic behavior of the individual parts of a functioning organism. As each type of tissue from different organs is differently perfused, a broad variability in the intrinsic transverse relaxation should be expected from one organ to another.[27] Hence, to appreciate the impact of TMNC accumulation in a particular tissue, the detected T_2 values were compared with the respective averaged readout signal of the same tissue from untreated mice (control). A relevant amount of TMNC in the MCF-7 tumor at 5 h postinjection was inferred by the increase in $1/T_2$ of this sample, remarkably higher than the control. The gradual increment in $1/T_2$ over time was an index of the progressive accumulation of iron in the tumor and confirmed that TMNC was incorporated by MCF-7 cells and forwarded to the degradation pathways (Figure 3b).

To corroborate our observation that the drop of fluorescence in the tumor was actually due to the degradation of the nanocomplex inside the cells and to obtain a more accurate quantification of nanocrystals in the tumor, we repeated the experiment with perfused mice, where blood supply was absent. Spectrofluorimetric and relaxometric analyses of tumor lysates are reported in Supporting Information (Figure S4).

Active Targeting or Passive Delivery? As a final confirmation that the *in vivo* localization of TMNC in MCF-7 tumors was actually due to an active targeting mediated by its specific interaction with HER2 receptors, we investigated the localization of injected nanocrystals in mice bearing HER2-negative MDA cells. This tumor model was previously validated as a negative control for TMNC specificity in cell cultures.[18] The localization of AF660-TMNC was determined 5 h after injection, which corresponded to the time of maximal fluorescence in

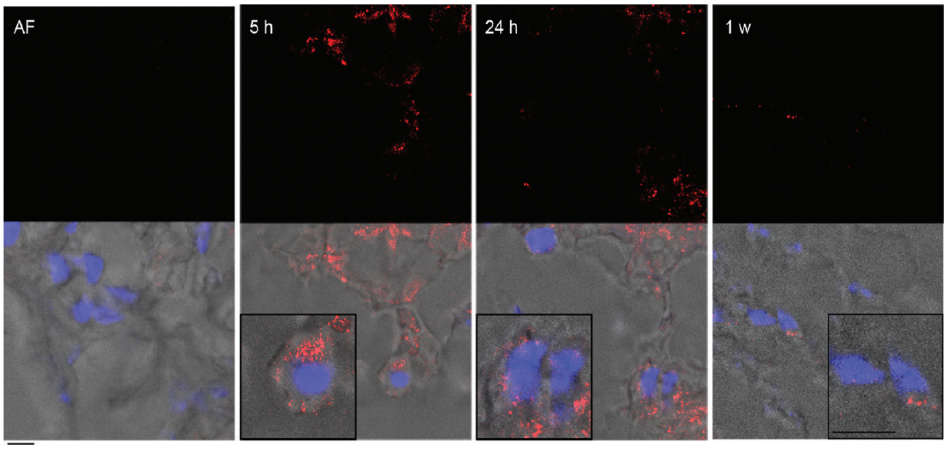

Figure 6. Confocal laser scanning micrographs (single optical sections) of cryosections obtained from MCF-7 tumors at 5 h, 24 h, and 1 week postinjection of AF660-TMNC, and then counterstained with DAPI for nuclei detection. Autofluorescence sample (AF) is a MCF-7 tumor from noninjected mice. The confocal images of nanocrystals (red) have been overlaid on the corresponding bright-field images reporting nuclei (blue). A high magnification of representative cells can be observed in the insets. Scale bars = 10 μm.

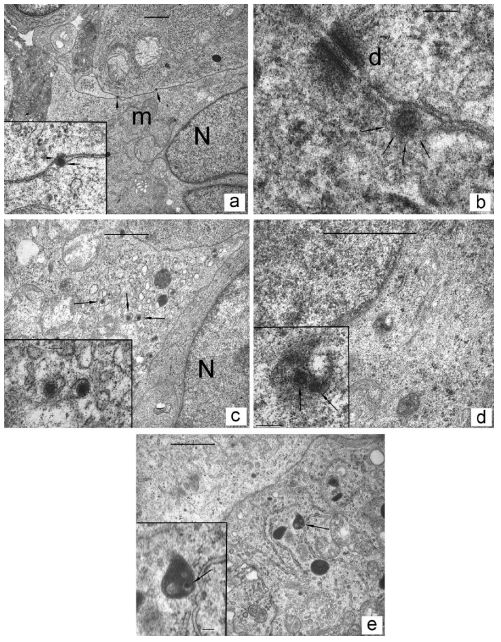

Figure 7. TEM images of MCF-7 tumors isolated at 5 h (a,b), 24 h (c,d), and 1 week (e) postinjection of AF660-TMNC. At 5 h, (a) two nanocrystals (arrows) are interposed between the membranes of two adjacent cells. At a higher magnification (inset), it is evident the close interaction of nanocrystal with membrane (arrows), which invaginates at the binding site level (b). At 24 h, nanocrystals are compartmentalized (arrows) in endosomes (c) and lysosomes (d) and, after 1 week, only in lysosomes (e): m, mitochondria; N, nucleus; d, desmosome. Scale bars = 1 μm (a,c,d,e), 100 nm (b and insets).

MCF-7 tumors. *In vivo* and *ex vivo* CCD camera observations of MDA xenografts (Figure 4a,b) showed a very weak Epf in this cancer model compared to MCF-7, and the averaged Epf intensity of the isolated MDA tumor was significantly lower ($P < 0.05$ by Student's *t*-test) than that measured in MCF-7 tumors, although the biodistribution of TMNC in the two experimental models was comparable (Figures S5 and S6). Moreover, the fluorescence intensity of MDA lysate was one-fifth the value measured in MCF-7 lysates in one of the three tumors analyzed, while in the supplementary two samples was below the detection limit.

Immunohistochemical Analysis of HER2 Expression in Tumor Tissues. Whereas it is well-known that HER2 overexpression is essentially a result of erbB2 gene amplification, it has recently been recognized that erbB2 levels are also regulated on the protein level.[28] To assess the extent of residual receptor expression after treatment of diseased mice with TMNC, we performed an immunohistochemical analysis of tumor tissues drawn at the same time stages of the other experiments. In the absence of TMNC (Figure 5a), we observed a diffuse and strong membrane staining in more than 60% of the neoplastic cells (immunohistochemical score, IHC, +++). At 5 h after TMNC injection (Figure 5b), most of the neoplastic cells were c-erb-2-negative or had a weak and incomplete membrane staining (IHC+). Only a small percentage of the neoplastic elements were scored as c-erb-2 IHC++ (weak yet complete membrane staining). At 24 h and 1 week (Figure 5c,d, respectively), the tumor had a reduced c-erb-2 expression: in these samples, only a minimal residual amount of c-erb-2-positive cells was recovered (IHC+). These results confirm the direct involvement of HER2 in the mechanism of TMNC internalization and suggest a potential application of TMNC in immunoadjuvant or even neoadjuvant therapy exploiting their capability to interfere with HER2-mediated signaling.[29]

Fate of Captured TMNC in MCF-7 Cells. A confocal microscopy examination of tumor cryosections indicated that AF660-TMNC came into contact with the plasma membrane of cells to be subsequently internalized. Figure 6, reporting a single *z*-plane in the cells, in which nuclei are focused, shows that TMNC was interacting with cell surface at 5 h. An intense fluorescence signal

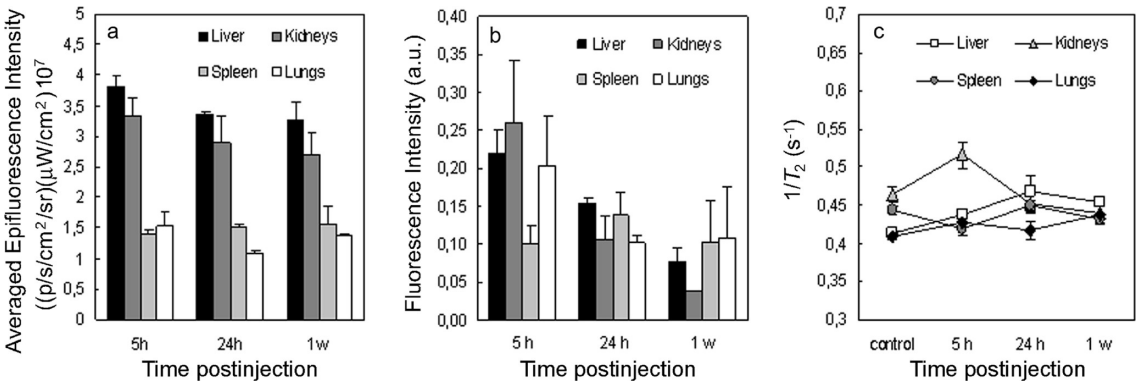

Figure 8. Averaged epifluorescence intensity of isolated liver, kidneys, spleen, and lungs (a), and fluorescence intensity (b) and inverse relaxation time (c) of organ lysates at 5 h, 24 h, and 1 week postinjection of AF660-TMNC. Mean ± SE of three different samples for each experimental time.

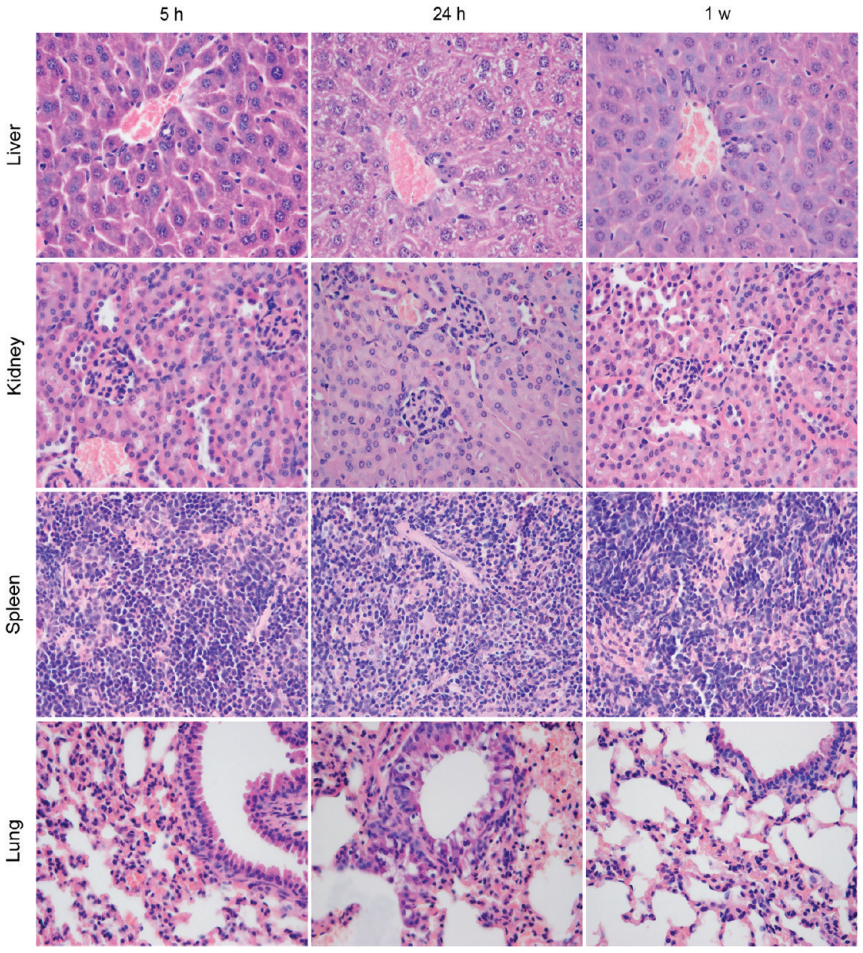

Figure 9. Histopathological analysis of tissue samples. No histological lesions in liver, kidneys, and spleen. A mild inflammatory interstitial infiltrate in all lung samples; a mild hyperplastic reaction of the bronchial epithelium is observed in 24 h lung sample (center of the figure). Hematoxylin-eosin, OM 20×.

was observed in correspondence with the cells, and the staining was mainly localized at the membrane level, as evidenced in the high-magnification image of a single cell cross section. Within 24 h, TMNC was endocytosed by tumor cells, as indicated by the presence of labeled spots deep in the cytoplasm and nearby the nucleus. Fluorescence intensity appeared strongly reduced in tumors isolated after 1 week, where only rare spots were still detectable in close proximity to the nucleus. TEM images provided compelling evidence that TMNC was captured by the plasma membrane of MCF-7 cells within the first 5 h (Figure 7a) followed by membrane invagination, which likely reflects the binding to the target receptors activating the process of

internalization (Figure 7b). After 24 h, TMNC was recovered inside the cytoplasm, compartmentalized in endosomes (Figure 7c) and lysosomes (Figure 7d), suggesting that it was subjected to a typical endocytic pathway upon incorporation by the cell.[30] The presence of TMNC in lysosomes clearly indicates that the degradation of nanocomplexes began within the first 24 h from their injection, thus justifying the drop in fluorescence observed in intact tumors and lysates at this time of exposure. The degradation process progressed over the following days, as indicated by the presence of nanocrystals only in lysosomes after 1 week (Figure 7e).

Analysis of Biodistribution of TMNC in Tumor-Bearing Mice. To evaluate the biodistribution of injected TMNC in mice, some model organs have been monitored by a CCD camera as described above for extracted tumors. The Epf images of liver, kidneys, spleen, and lungs were determined 5 h, 24 h, and 1 week after AF660-TMNC injection. The averaged Epf intensities for each imaged organ (Figure S6) are represented in Figure 8a. Epf intensity was remarkably higher in liver and kidneys, and a detectable tendency to decrease over time in these two organs was apparent.

A more quantitative assessment of TMNC in each individual organ was performed by measuring the fluorescence intensity of lysates. A comparison between the different organs was possible by normalizing the fluorescence values to the total protein content (Figure 8b). The results obtained confirmed a preferential distribution of TMNC in liver and kidneys after 5 h, and an appreciable fluorescence was also recovered in lungs, although no significant labeling was observed in *ex vivo* imaging, probably due to a deeper penetration of labeled nanocrystals in this tissue. Moreover, Figure 8b clearly shows the progressive decrease of intensity in liver and kidneys: after 1 week from TMNC injection, the fluorescence intensity of liver and kidneys was reduced to about one-third and one-fifth, respectively, of the values recorded at 5 h. A relaxometric analysis of the same organ lysates confirmed that nanocrystals were present in liver and kidneys at 5 h postinjection detected as an increase in $1/T_2$ compared to the respective controls (Figure 8c). On one hand, the increase over time in the liver of magnetically active content owed to the metal core combined with the decrease in fluorescence intensity associated with the bioorganic corona suggests that TMNC was internalized and decomposed by this organ exploiting its detoxification role.[31,32] On the other hand, the gradual decrease of $1/T_2$ values in the kidneys follows the drop of Epf intensity in these organs. This effect might be interpreted as the result of TMNC excretion, in contrast with previous observations that a size limit of 5−10 nm is allowed for particle excretion by the kidneys.[33] A possible explanation could be that TMNC were provisionally captured by the kidneys while being delivered down the blood flow, until they reached their final destination at the tumor site or in the liver. Alternatively, the gradual dissolution of the particles could result in another iron phase with different magnetic properties, therefore leading to different NMR contrast. Whatever the actual interpretation, TMNC did not accumulate in the kidneys for a long time. According to the T_2 values measured in spleen and lung lysates (Figure 8c), we can assume that iron content was detectable in lungs at 5 h and exhibited only small variations over the experimental time. This result is in agreement with previous studies describing distribution of intravenously injected nanoparticles in lungs.[34,35] On the other hand, the metal appeared surprisingly undetectable in the spleen.

This behavior was confirmed also with perfused mice, demonstrating that this effect could not be attributed to paramagnetic inhomogeneities from circulating blood (Figure S7).

Assessment of TMNC Toxicity. In order to investigate the possible toxic effects of TMNC on nontarget organs,[36] we performed a histopathological examination of liver, kidneys, spleen, and lungs isolated 5 h, 24 h, and 1 week after TMNC injection (Figure 9). No histological lesions were found in liver, kidneys, and spleen at all observed times. Lung tissues were characterized by a focal and mild inflammatory infiltrate localized at the interstice. Bronchi were spared except for samples at 24 h, in which an early hyperplastic reaction of the epithelium was observed. This acute alteration was transitory and regressed within a few days. Samples at 1 week exhibited no traces of lesions.

TMNC safety has been also verified by investigating liver and kidney functionalities in serum (Table S1). Dosage of aspartate transaminase (AST), alanine transaminase (ALT), urea, and creatinine was performed by specific commercial assay kits (BioAssay Systems, USA). An apparent alteration of renal and hepatic functionality was observed in the first 5 h, but it was completely restored within the following 24 h.

CONCLUSION

In summary, we have synthesized a PEGylated hybrid magnetic nanoparticle functionalized with fluorescently labeled trastuzumab (TMNC) with a control on the antibody orientation on the nanoparticle surface to optimize the targeting efficiency. These nanoparticles proved to be highly effective in selectively targeting HER2-positive breast cancer cells *in vivo* and thus are expected to have potential for monitoring metastatic lymph nodes. A multifaceted bioanalytical approach, combining fluorescence, magnetic relaxivity, transmission electron microscopy, and histological experiments *in vivo* and *ex vivo*, has demonstrated that TMNC (1) prevalently accumulated at the tumor by active targeting and at the liver after an initial broad distribution, (2) was endocytosed by the cells of tumor tissues

following a lysosomal pathway of degradation, and (3) did not result in permanent damage of healthy tissues, although an initial bronchial inflammation was recovered, which will need further investigation in the future. Our results suggest that TMNC is internalized by HER2 receptor-mediated endocytosis, leading to the capture of the TMNC−HER2 complex by lysosomes, followed by rapid degradation of the bioorganic corona, while the inorganic core is expected to be more slowly decomposed. Most importantly, this work highlights the necessity of using different approaches for nanoparticle tracking *in vivo*, as we have demonstrated that organic fluorophores utilized for fluorescent labeling of immobilized biomolecules could be rapidly metabolized upon internalization of the TMNC−HER2 complex, while metal components of nanoparticles kept accumulating in the tumor. Immunohistochemical analysis has provided evidence that TMNC was able to saturate HER2 monomers expressed on cell surface of the tumor tissue, thus eliciting the rapid receptor degradation, which is expected to strongly interfere with signaling processes promoted by this receptor. This behavior paves the way to explore the potential of TMNC as an immunotheranostic agent, which might find application in presurgical neoadjuvant treatments. The *in vivo* molecular approach described here may provide a new perspective in the design of the next generation of multifunctional nanohybrid systems for biomedical application.

MATERIALS AND METHODS

TMNC Production. Magnetic nanocrystals (MNCs) were synthesized and functionalized with an individual B domain of protein A (spaBC3), as described in our previous work with modifications.[18] Briefly, 8 nm iron oxide nanoparticles coated with oleic acid dissolved in chloroform (84 mg, 4.3 mL) were diluted with chloroform (20 mL) and were treated with an aqueous solution of tetramethylammonium hydroxide (TMAOH, 2.4 g in 80 mL) overnight under vigorous stirring at room temperature.[37] The organic solution containing the surfactant was removed by centrifugation at 1000*g* (3 min). The aqueous solution of TMAOH-coated MNC was mixed with 0.1 M *N*-phosphonomethyl iminodiacetic acid phosphonate (PMIDA, 500 mg) dissolved in an aqueous ammonia solution in order to promote ligand exchange. Carboxyl groups onto the surface of the resulting nanoparticles were converted into amine ends by reaction with the bifunctional diamino linker 2,2′-(ethylenedioxy)bisethylamine (EDBE, 284 μL) *via* *N*-(3-dimethylaminopropyl) *N*-ethylcarbodiimide hydrochloride (EDC, 16.2 mg) activation. *N*-Succinimidyl-3-[2-piridyldithio]propionate (SPDP, 4.3 mg) dissolved in dry DMSO (0.75 mL) was conjugated to MNC *via* NHS ester. The resulting thiol-reactive nanoparticles (1 mg) were incubated in the presence of spaBC3 (0.5 mg), obtaining the binding of 0.1 mg of spaBC3. The amount of spaBC3 bound was determined by protein quantification of supernatants. The remaining PDP functional groups were saturated with excess PEG_{500}-SH. Trastuzumab was labeled with AlexaFluor660 dye (Invitrogen, Carlsbad, CA) according to manufacturer's protocol. Trastuzumab conjugation on nanoparticles was performed by incubating nanoparticles (1 mg) at room temperature for 2 h in the presence of labeled Trastuzumab (0.3 mg), obtaining the binding of 0.1 mg of Tz. The amount of Tz bound was determined by protein quantification of supernatants.

Cell Culture and Xenograft Tumor Models. MCF-7 cells were grown in 50% Dulbecco's modified Eagle's medium (DMEM), 50% F12 (EuroClone Celbio, Milan, Italy) supplemented with 10% (v/v) fetal bovine serum (Hyclone Celbio, Milan, Italy), L-glutamine (2 mM), penicillin (50 UI mL^{-1}), and streptomycin (50 mg mL^{-1}) at 37 °C under a humidified 95%:5% (v/v) mixture of air and CO_2. MDA-MD-468 was purchased by ATCC and cultured in Dulbecco's modified Eagle's medium supplemented with 10% (v/v) fetal bovine serum (Hyclone Celbio, Milan, Italy), L-glutamine (2 mM), penicillin (50 UI mL^{-1}), and streptomycin (50 mg mL^{-1}) in the same condition of growth. Eight week old female Balb/c nude mice were anesthetized by i.p. injection of 20 mg mL^{-1} of Avertin, and estrogen pellets were placed s.c. on the back of the mouse's neck by using a trocar. All tumor injections were done 2 days after this procedure. MCF-7 and MDA (10×10^6 cell for each animals) were suspended in growth medium and mixed with Matrigel high factor (BD, Biosciences) in 3:1 ratio and injected into mammary fat pad of Balb/C nude mice (Charles River). Animals were observed at least three times per week, and tumor formation was recorded; tumors were allowed to grow up to 7−10 mm in diameter before nanocomplex injection and imaging.

Magnetic Resonance Imaging. MRI experiments were performed on a 7-T Bruker Biospec 70/30 USR scanner, 30 cm horizontal bore (Bruker BioSpin, Ettlingen, Germany) equipped with a BGA12S (200 mT/m) gradient system and with a 35 mm quadrature volume coil for RF excitation and signal reception. Mice were anaesthetized with 1.5−2% isoflurane (60:40 N_2O/O_2 (vol/vol), flow rate 0.8 L/min). To detect the depth of anesthesia and the animal health condition during the MRI study, the respiratory rate and temperature were monitored by a pneumatic and rectal sensor, respectively. Animals were positioned on an animal bed equipped with a nosecone for gas anesthesia and a three-point-fixation system (tooth-bar and ear-plugs). A 3-orthogonal plane gradient echo tripilot scan was used as a geometric reference to locate the kidneys and the bladder, from which to choose the sections. T_2-weighted images (Coronal; RARE factor = 8, TR = 2 s, TE = 34.8 ms, inter echo time = 11.6 ms, FOV = 4×3.4 cm^2, data matrix 300×256, slice thickness = 1 mm, trigger on with respiration gate = 2 s, NA = 8) were acquired to visualize anatomical details (liver, kidneys, bladder, tumor). T_2*-weighted images (Coronal, Multi Gradient Echos, flip angle = 30°, TR = 800 ms, numbers of echoes = 4, first TE = 3 ms, echo spacing = 5 ms, FOV = 3×3 cm^2, data matrix 256×256, slice thickness = 1 mm, trigger on with respiration gate = 800 ms, NA = 1; axial; FLASH flip angle = 30°, TR = 350 ms, TE = 5.4 ms, FOV = 2.2×2.2 cm^2, data matrix 256×256, slice thickness = 1 mm, NA = 1) were acquired to visualize the susceptibility artifacts due to the presence of iron. To obtain T_2 and T_2* map, MSME and MGE sequences were carried out, respectively (MSME, axial, TR = 3.2 s, numbers of echoes = 20, echo spacing = 10.7 ms, FOV = 2.2×2.2 cm^2, data matrix 256×256, slice thickness = 1.5 mm, NA = 1; MGE, axial, flip angle = 30°, TR = 1.5 s, numbers of echoes = 18, first TE = 4 ms, echo spacing = 6 ms, FOV = 2.2×2.2 cm^2, data matrix 256×256, slice thickness = 1.5 mm, NA = 2). From these images, the tumor was manually segmented and maps were computed by the Paravision 5.1 Bruker software.

TMNC Injection and *In Vivo* and *Ex Vivo* Fluorescence Imaging. Mice were immobilized in a restrainer specifically designed for tail vein injections (2 biological instrument, Varese, Italy) and 250 μL of AF660-TMNC, 0.4 mg/mL was injected (5 μg/g body weight). Fluorescence imaging was performed on a IVIS Lumina II CCD camera (Calipers Life Sciences, UK) at 5 h, 24 h, and 1 week postinjection. Animals were anesthetized by i.p. injection of

20 mg mL^{-1} of Avertin and placed in CCD camera at 37 °C. Images were acquired with a Cy5.5 emission filter, while excitation was scanned from 570 to Cy5.5, and mice autofluorescence was removed by spectral unmixing. After *in vivo* acquisitions, mice were sacrificed, and dissected tumors and organs were analyzed with a CCD camera, as described above for the whole animals.

Confocal Microscopy of Cryosections. MCF-7 tumors were isolated and fixed in 4% paraformaldehyde solution for 3 h, washed in PBS, and embedded in OCT for freezing in liquid nitrogen. Ten micrometer thick tumor cryosections were air-dried at room temperature for 1 h, rinsed with PBS, and counterstained with DAPI (diluted 2:1000 in PBS 0.1% Saponin) for 20 min in the dark. After three washes in PBS, sections were mounted in ProLong Gold antifade reagent (Invitrogen) to be observed under a Leica TCS SPE confocal microscope (Leica Microsystems, Wetzlar, Germany). Confocal images were acquired at Fondazione Filarete, Milano, Italia.

Tissue Concentration of AF660-TMNC in Lysates. To obtain tissue samples, mice were sacrificed at different time points after injection with nanoparticles. For fluorescence intensity measurements, liver, spleen, kidney, and lung were excised, weighed, and homogenized with ultraturrax with homogenization buffer (0.32 M sucrose, 100 mM hepes, pH 7.4). The homogenate tissue lysates were centrifuged, and supernatant was resuspended in lysis buffer at a final concentration of 50 mM Tris, pH 7.4, and SDS 1% and incubated for 30 min at 4 °C on a rotator. The supernatant was used for bicinchonic acid (BCA, Pierce, CA) protein assay and for fluorescence measurement with GloMax Multi Detection System (Promega).

T_2 Measurements of Lysates. T_2 relaxation times were performed at a temperature of 313 K using a Bruker Minispec mq20 system (Ettlingen, Gerrmany) working with ^{1}H at 20 MHz magnetic field with the following parameters: Carr-Purcell-Meiboom-Gill pulse sequence, 1000 echoes with a 20 ms echo times and 2 s repetition time. Before T_2 measurements, lysates were diluted at a concentration of 1.5 mg mL^{-1} and introduced using 10 mm NMR spectroscopy tubes prewarmed at 40 °C. T_2 values were acquired after thermal equilibration.

Histopathological Analysis. Liver, kidneys, spleen, and lung samples obtained from Balb/c mice were fixed in 10% buffered formalin for at least 48 h and embedded in paraffin. Three micrometer sections were cut, stained with hematoxylin and eosin, and examined blindly.

Ultrastructural Analysis (TEM). Small portions of MCF-7 tumor samples were fixed in 2.5% glutaraldehyde in 0.1 M phosphate buffer, pH 7.2, for 2 h. After one rinsing with phosphate buffer, specimens were postfixed in 1.5% osmium tetroxide for 2 h, dehydrated by 70, 90, and 100% EtOH, and embedded in epoxy resin (PolyBed 812 Polysciences Inc., USA). Ultrathin sections were stained with uranyl acetate and lead citrate and examined by means of a transmission electron microscope (Zeiss EM109).

Immunohistochemistry. Three micrometer thick paraffin-embedded tissues were cut, deparaffinized in xylene, and rehydrated in ethanol. Microwave oven pretreatment was performed (pH 8.0, EDTA buffer, 2 × 5′). Immunohistochemistry was performed by using a polyclonal antibody rabbit anti-human c-erb-2 oncoprotein (1:1000 dilution, DakoCytomation, 2 h incubation). The reaction was revealed by means of supersensitive nonbiotin detection system (BioGenex) and diaminobenzidine as chromogen.

Acknowledgment. We thank A. Salvadè for help in cell analyses, I. Zucca for acquisition of MR images, E. Pesenti for mice perfusion, and E. Trabucchi for helpful discussions. This work was partly supported by "Assessorato alla Sanità", Regione Lombardia, and Sacco Hospital (NanoMeDia Project), the "Fondazione Romeo ed Enrica Invernizzi", and the Italian Association for Cancer Research. M.C. and S.M. acknowledge "Centro di Microscopia Elettronica per lo sviluppo delle Nanotecnologie applicate alla medicina" (CMENA, University of Milan) for doctoral and postdoctoral fellowships, respectively.

Supporting Information Available: TEM image of nanocrystals, T_2* maps, CCD camera images of organs and epifluorescence distribution. This material is available free of charge *via* the Internet at http://pubs.acs.org.

REFERENCES AND NOTES

1. Weissleder, R.; Pittet, M. J. Imaging in the Era of Molecular Oncology. *Nature* **2008**, *452*, 580–589.
2. de Vries, I. J. M.; Lesterhuis, W. J.; Barentsz, J. O.; Verdijk, P.; van Krieken, J. H.; Boerman, O. C.; Oyen, W. J. G.; Bonenkamp, J. J.; Boezeman, J. B.; Adema, G. J.; *et al.* Magnetic Resonance Tracking of Dendritic Cells in Melanoma Patients for Monitoring of Cellular Therapy. *Nat. Biotechnol.* **2005**, *23*, 1407–1413.
3. Evgenov, N. V.; Medarova, Z.; Dai, G.; Bonner-Weir, S.; Moore, A. *In Vivo* Imaging of Islet Transplantation. *Nat. Med.* **2006**, *12*, 144–148.
4. McMasters, K. M.; Tuttle, T. M.; Carlson, D. J.; Brown, C. M.; Noyes, R. D.; Glaser, R. L.; Vennekotter, D. J.; Turk, P. S.; Tate, P. S.; Sardi, A.; *et al.* Sentinel Lymph Node Biopsy for Breast Cancer: A Suitable Alternative to Routine Axillary Dissection in Multi-institutional Practice when Optimal Technique Is Used. *J. Clin. Oncol.* **2000**, *18*, 2560–2566.
5. Yang, L.; Peng, X.-H.; Wang, Y. A.; Wang, X.; Cao, Z.; Ni, C.; Karna, P.; Zhang, X.; Wood, W. C.; Gao, X.; *et al.* Receptor-Targeted Nanoparticles for *In Vivo* Imaging of Breast Cancer. *Clin. Cancer Res.* **2009**, *15*, 4722–4732.
6. Kim, J.; Piao, Y.; Hyeon, T. Multifunctional Nanostructured Materials for Multimodal Imaging, and Simultaneous Imaging and Therapy. *Chem. Soc. Rev.* **2009**, *38*, 372–390.
7. Riehemann, K.; Schneider, S. W.; Luger, T. A.; Godin, B.; Ferrari, M.; Fuchs, H. Nanomedicine—Challenge and Perspectives. *Angew. Chem., Int. Ed.* **2009**, *48*, 872–897.
8. Lu, A.-H.; Salabas, E. L.; Schüth, F. Magnetic Nanoparticles: Synthesis, Protection, Functionalization, and Application. *Angew. Chem., Int. Ed.* **2007**, *46*, 1222–1244.
9. Pellegrino, T.; Manna, L.; Kudera, S.; Liedl, T.; Koktysh, D.; Rogach, A. L.; Keller, S.; Radler, J.; Natile, G.; Parak, W. J. Hydrophobic Nanocrystals Coated with an Amphiphilic Polymer Shell: A General Route to Water Soluble Nanocrystals. *Nano Lett.* **2004**, *4*, 703–707.
10. Haun, J. B.; Devaraj, N. K.; Hilderbrand, S. A.; Lee, H.; Weissleder, R. Bioorthogonal Chemistry Amplifies Nanoparticle Binding and Enhances the Sensitivity of Cell Detection. *Nat. Nanotechnol.* **2010**, *5*, 660–665.
11. Kampmeier, F.; Ribbert, M.; Nachreiner, T.; Dembski, S.; Beaufils, F; Brecht, A.; Barth, S. Site-Specific, Covalent Labeling of Recombinant Antibody Fragments *via* Fusion to an Engineered Version of 6-*O*-Alkylguanine DNA Alkyltransferase. *Bioconjugate Chem.* **2009**, *20*, 1010–1015.
12. Kumar, S.; Aaron, J.; Sokolov, K. Directional Conjugation of Antibodies to Nanoparticles for Synthesis of Multiplexed Optical Contrast Agents with Both Delivery and Targeting Moieties. *Nat. Protoc.* **2008**, *3*, 314–320.
13. Harisinghani, M. G.; Barentsz, J.; Hahn, P. F.; Deserno, W. M.; Tabatabaei, S.; van de Kaa, C. H.; de la Rosette, J.; Weissleder, R. Noninvasive Detection of Clinically Occult Lymph Node Metastases in Prostate Cancer. *N. Engl. J. Med.* **2003**, *348*, 2491–2499.
14. Memarsadeghi, M.; Riedl, C. C.; Kaneider, A.; Galid, A.; Rudas, M.; Matzek, W.; Helbich, T. H. Axillary Lymph Node Metastases in Patients with Breast Carcinomas: Assessment with Nonenhanced *versus* USPIO-Enhanced MR Imaging. *Radiology* **2006**, *241*, 367–377.
15. Jiang, W.; Kim, B. Y. S.; Rutka, J. T.; Chan, W. C. W. Nanoparticle-Mediated Cellular Response is Size-Dependent. *Nat. Nanotechnol.* **2008**, *3*, 145–150.
16. Chen, J.; Irudayaraj, J. Quantitative Investigation of Compartmentalized Dynamics of ErbB2 Targeting Gold Nanorods in Live Cells by Single Molecule Spectroscopy. *ACS Nano* **2009**, *3*, 4071–4079.
17. Peer, D.; Karp, J. M.; Hong, S.; Farokhzad, O. C.; Margalit, R.; Langer, R. Nanocarriers as an Emerging Platform for Cancer Therapy. *Nat. Nanotechnol.* **2007**, *2*, 751–760.
18. Mazzucchelli, S.; Colombo, M.; De Palma, C.; Salvadè, A.; Verderio, P.; Coghi, M. D.; Clementi, E.; Tortora, P.; Corsi, F.; Prosperi, D. Single-Domain Protein A-Engineered Magnetic Nanoparticles: Toward a Universal Strategy to Site-Specific Labeling of Antibodies for Targeted Detection of Tumor Cells. *ACS Nano* **2010**, *4*, 5693–5702.

19. Colombo, M.; Corsi, F.; Foschi, D.; Mazzantini, E.; Mazzucchelli, S.; Morasso, C.; Occhipinti, E.; Polito, L.; Prosperi, D.; Ronchi, S.; *et al.* HER2 Targeting as a Two-Sided Strategy for Breast Cancer Diagnosis and Treatment: Outlook and Recent Implications in Nanomedical Approaches. *Pharmacol. Res.* **2010**, *62*, 150–165.
20. Ménard, S.; Tagliabue, E.; Campiglio, M.; Pupe, S. M. Role of HER2 Gene Overexpression in Breast Carcinoma. *J. Cell Physiol.* **2000**, *182*, 150–162.
21. Yezhelyev, M. V.; Gao, X.; Xing, Y.; Al-Hajj, A.; Nie, S.; O'Regan, R. M. Emerging Use of Nanoparticles in Diagnosis and Treatment of Breast Cancer. *Lancet Oncol.* **2006**, *7*, 657–667.
22. Cheon, J.; Lee, J.-H. Synergistically Integrated Nanoparticles as Multimodal Probes for Nanobiotechnology. *Acc. Chem. Res.* **2008**, *41*, 1630–1640.
23. Chari, R. V. J. Targeted Cancer Therapy: Conferring Specificity to Cytotoxic Drugs. *Acc. Chem. Res.* **2008**, *41*, 98–107.
24. Bardhan, R.; Chen, W.; Bartels, M.; Perez-Torres, C.; Botero, M. F.; McAninch, R. W.; Contreras, A.; Schiff, R.; Pautler, R. G.; Halas, N. J.; *et al.* Tracking of Multimodal Therapeutic Nanocomplexes Targeting Breast Cancer *in Vivo*. *Nano Lett.* **2010**, *10*, 4920–4928.
25. Clifford, A.; Hudis, M. D. Trastuzumab—Mechanism of Action and Use in Clinical Practice. *N. Engl. J. Med.* **2007**, *357*, 39–51.
26. Wuang, S. C.; Neoh, K. G.; Kang, E.-T.; Pack, D. W.; Leckband, D. E. HER-2-Mediated Endocytosis of Magnetic Nanospheres and the Implications in Cell Targeting and Particle Magnetization. *Biomaterials* **2008**, *29*, 2270–2279.
27. Mahmoudi, M.; Hosseinkhani, H.; Hosseinkhani, M.; Boutry, S.; Simchi, A.; Journeay, W. S.; Subramani, K.; Laurent, S. Magnetic Resonance Imaging Tracking of Stem Cells *in Vivo* Using Iron Oxide Nanoparticles as a Tool for the Advancement of Clinical Regenerative Medicine. *Chem. Rev.* **2011**, *111*, 253–280.
28. Lam, P. B.; Burga, L. N.; Wu, B. P.; Hofstatter, E. W.; Ping Lu, K.; Wulf, G. M. Prolyl Isomerase Pin1 Is Highly Expressed in Her2-Positive Breast Cancer and Regulates ErbB2 Protein Stability. *Mol. Cancer* **2008**, *7*, 91–102.
29. Mauri, D.; Pavlidis, N.; Ioannidis, J. P. Neoadjuvant *versus* Adjuvant Systemic Treatment in Breast Cancer: A Meta-Analysis. *J. Natl. Cancer Inst.* **2005**, *97*, 188–194.
30. Corsi, F.; De Palma, C.; Colombo, M.; Allevi, R.; Nebuloni, M.; Ronchi, S.; Rizzi, G.; Tosoni, A.; Emilio, T.; Emilio, C.; Prosperi, D. Towards Ideal Magnetofluorescent Nanoparticles for Bimodal Detection of Breast-Cancer Cells. *Small* **2009**, *5*, 2555–2564.
31. Sadauskas, E.; Danscher, G.; Stoltenberg, M.; Vogel, U.; Larsen, A.; Wallin, H. Protracted Elimination of Gold Nanoparticles from Mouse Liver. *Nanomedicine* **2009**, *5*, 162–169.
32. Briley-Saebo, K.; Bjørnerud, A.; Grant, D.; Ahlstrom, H.; Berg, T.; Mørk Kindberg, G. Hepatic Cellular Distribution and Degradation of Iron Oxide Nanoparticles Following Single Intravenous Injection in Rats: Implications for Magnetic Resonance Imaging. *Cell Tissue Res.* **2004**, *316*, 315–23.
33. Choi, H. S.; Liu, W.; Misra, P.; Tanaka, E.; Zimmer, J. P.; Itty Ipe, B.; Bawendi, M. G.; Frangioni, J. V. Renal Clearance of Quantum Dots. *Nat. Biotechnol.* **2007**, *25*, 1165–1170.
34. Lankveld, D. P. K; Oomen, A. G.; Krystek, P.; Neigh, A.; Troost-de Jong, A.; Noorlander, C. W.; Van Eijkeren, J. C. H.; Geertsma, R. E.; De Jong, W. H. The Kinetics of the Tissue Distribution of Silver Nanoparticles of Different Sizes. *Biomaterials* **2010**, *31*, 8350–8361.
35. Cole, A. J.; David, A. E.; Wang, J.; Galban, C. J., Yang, V. C. Magnetic Brain Tumor Targeting and Biodistribution of Long-Circulating PEG-Modified, Cross-Linked Starch-Coated Iron Oxide Nanoparticles. *Biomaterials* **2011**, *32*, 6291−6301.
36. Kim, J. S.; Yoon, T. J.; Yu, K. N.; Kim, B. G.; Park, S. J.; Kim, H. W.; Lee, K. H.; Park, S. B.; Lee, J. K.; Cho, M. H. Toxicity and Tissue Distribution of Magnetic Nanoparticles in Mice. *Toxicol. Sci.* **2006**, *89*, 338–347.
37. Liong, M; Shao, H.; Haun, J. B.; Lee, H.; Weissleder, R. Carboxymethylated Polyvinyl Alcohol Stabilizes Doped Ferrofluids for Biological Applications. *Adv. Mater.* **2010**, *22*, 5168–5172.